Marco Antônio Haas Vogt

ELUCIDATION OF THE KINETICS OF THE REDOX REACTION OF HIGHLY REDUCIBLE CeO_{2-x} ($0 < x < 0.5$) NANOPARTICLES

Porto Alegre, RS – Brazil

November, 2020

Marco Antônio Haas Vogt

ELUCIDAÇÃO DA CINÉTICA DA REAÇÃO REDOX DE NANOPARTÍCULAS ALTAMENTE REDUTÍVEIS DE CeO_{2-x} ($0 < x < 0,5$)

Dissertação realizada sob a orientação do Prof. Dr. Fabiano Bernardi e apresentada ao Instituto de Física da UFRGS, em preenchimento parcial dos requisitos para obtenção do título de Mestre em Física.

Universidade Federal do Rio Grande do Sul

Instituto de Física

Programa de Pós-Graduação em Física

Orientador: Prof. Dr. Fabiano Bernardi

Porto Alegre, RS – Brasil

Novembro, 2020

ACKNOWLEDGMENTS

To my parents and my brother, for all the support they gave me to make this achievement possible.

To all my friends who made this journey less stressful.

To Prof. Dr. Fabiano Bernardi for the patience, friendship and advisement.

To Prof. Dra. Fernanda Poletto and Francielli Lobato from IQ-UFRGS for synthesizing the samples used in this work.

To LNLS for providing access to the Brazilian Synchrotron in order to perform the in situ XRD, XANES and EXAFS measurements presented in this work.

To CNANO for providing the ex situ XRD measurements presented in this work.

To CMM for providing access to TEM microscope in order to obtain the images of the nanoparticles presented in this work.

And to CAPES for the Master fellowship that made this achievement possible.

“However difficult life may seem, there is always something you can do and succeed at”

Stephen Hawking

RESUMO PARA PÚBLICO LEIGO

O óxido de cério é um composto químico que vem sendo muito estudado devido ao seu alto potencial tecnológico para diversas aplicações. Ele é interessante por ser capaz de acelerar a velocidade de reações químicas, o que permite melhorar o desempenho de processos industriais. Uma importante característica do óxido de cério é a facilidade em capturar e doar oxigênio. Em trabalho prévio do grupo, foram produzidas estruturas de óxido de cério com alta capacidade de doar oxigênio para a atmosfera em temperaturas muito menores do que aquelas previamente descritas. Esta é uma característica muito desejada, pois permite minimizar os gastos energéticos de processos que envolvam reações químicas devido à maior velocidade com a qual eles ocorrem em temperaturas menores. Outra característica importante do óxido de cério é a sua estrutura cristalina, ou seja, como os átomos que constituem esse material estão posicionados no espaço no estado sólido. Dependendo de como esse átomos estão posicionados, a capacidade do óxido de cério de acelerar reações químicas muda. Em altas temperaturas, costuma-se induzir o óxido de cério a perder oxigênio para que sua atuação nas reações químicas seja otimizada. Essa perda de oxigênio afeta sua estrutura cristalina. O objetivo desta dissertação de mestrado foi entender de forma aprofundada como ocorre essa perda e também o ganho de oxigênio nas estruturas de óxido de cério previamente produzidas pelo grupo, sob condições determinadas. Observou-se que, quando há muitos átomos de oxigênio na estrutura e esta é exposta a monóxido de carbono a 900 ºC, a posição dos átomos de oxigênio fica deslocada em relação à original. Como consequência, passam a coexistir duas estruturas cristalinas diferentes no material: a original e aquela com os oxigênios deslocados. Quando esse material é resfriado abruptamente na presença de hélio (um gás inerte) ao invés de monóxido de carbono, ocorre um comportamento incomum de expansão da estrutura cristalina. Em geral, materiais de composições variadas contraem ao invés de expandir ao serem resfriados. O comportamento inusitado do óxido de cério ocorre porque, com resfriamento abrupto, os átomos de oxigênio migram entre as duas estruturas cristalinas coexistentes.

No caso de estruturas de óxido de cério com poucos átomos de oxigênio, observou-se que o tamanho médio da estrutura e a posição dos átomos no espaço desempenham um papel fundamental para elucidar como ocorre a perda de oxigênio. Em estruturas menores, a perda de oxigênio da superfície faz com que oxigênio interno desloque-se para esse espaço vago criado. Este processo ocorre várias vezes, até que atinja uma situação crítica que induz mudança no mecanismo dessa perda. Nesse ponto, passa a ocorrer contração da parte mais interna da estrutura. Essa contração faz com que o oxigênio interno que estava aprisionado ali saia da

estrutura, mesmo que não seja induzida a criação de novos espaços vagos na sua superfície. Já no caso de estruturas de óxido de cério maiores, observou-se um único mecanismo para a perda do oxigênio, baseado na contração da parte interna e consequente liberação do oxigênio aprisionado no seu interior. O estudo desenvolvido nesta disertação de mestrado ajudará a planejar materiais constituídos de óxido de cério mais eficientes para a indústria química.

ABSTRACT

The cerium oxide CeO_{2-x} ($0 < x < 0.5$) has been strongly studied due to the high technological potential for several applications. CeO_{2-x} presents high facility to change the oxidation state between Ce(III) ($x = 0.5$) and Ce(IV) ($x = 0$). The CeO_2 (Ce(IV) oxidation state) presents the fluorite-type crystal structure and Ce_2O_3 (Ce(III) oxidation state) presents the hexagonal one. In a previous work of the group, it was shown the possibility to control the surface area, mean diameter, and oxygen vacancies population of CeO_{2-x} nanoparticles by means of synthesis. Moreover, the cerium oxide nanoparticles synthesized showed high reducibility (high values for the Ce(III) fraction) in comparison to similar cerium oxide nanoparticles in the literature. The reduction reaction is routinely used to activate catalysts and, in some cases, it induces a phase transition with a consequent change in the catalytic properties. The main goal of this Master dissertation was to elucidate the kinetics of the redox reaction of highly reducible CeO_{2-x} nanoparticles.

The kinetics of the redox reaction of CeO_{2-x} nanoparticles of small x values was probed by in situ XRD measurements in CO atmosphere at a maximum temperature of 900 ºC. The measurements show the presence of a new crystal structure at 900 ºC, the cubic Cu_2Se-like one. During the cooling process in He atmosphere, this phase turns metastable and transforms back to the fluorite phase due to the high cooling rate applied, namely 15 ºC/min. The metastable phase presents a negative thermal expansion coefficient (α) for the temperature range of 580 ºC to 300 ºC. Using an approximation of Avrami's theory for non-isothermal processes, the kinetics of phase transition was studied. It shows that the phase transition occurs in 1D with the crystallization mechanism controlled by volume diffusion. Therefore, the formation of the fluorite phase during the cooling process is due to the O diffusion from the Cu_2Se-like to fluorite crystal structure, which explains the negative α value.

The kinetics of the redox reaction of CeO_{2-x} nanoparticles of high x values was probed by in situ XAS measurements at the Ce L_3 edge (5723 eV). In situ time-resolved XANES measurements for temperature ranges between 900 °C and 1020 °C in CO atmosphere were conducted. During heating in He atmosphere to the selected temperature, the synthesized nanoparticles presented an unexpected oxidation behavior at 450 ºC, which is associated to the formation of the triclinic crystal structure. After, at the selected temperature, it was observed that the mean size of the nanoparticles and the crystal structure play a key role to elucidate the kinetics behavior, influencing on the reduction mechanism. In general, the almost fully reduced CeO_{2-x} nanoparticles present the reduction mechanism D3 that changes to R2 for a given Ce(III)

fraction value. The D3 and R2 mechanisms are associated to bcc and hexagonal-rich phases, respectively. The exception is the case of nanoparticles with big mean size (> 50 nm) that presents the R3 mechanism independently of the Ce(III) fraction. For the first time it was obtained the activation energy of reduction reaction referent to the bcc phase of cerium oxide. The values are much higher than those typically found for the fluorite phase of cerium oxide. In situ EXAFS measurements in CO atmosphere at 500 ºC confirm the formation of the triclinic phase and the local atomic order around Ce atoms mainly depends on the synthesis parameters.

RESUMO

O óxido de cério CeO_{2-x} (0 < x < 0,5) vem sendo muito estudado devido ao seu alto potencial tecnológico para diversas aplicações. O CeO_{2-x} apresenta alta facilidade para alterar o estado de oxidação entre Ce(III) (x = 0,5) e Ce(IV) (x = 0). O CeO_2 (estado de oxidação Ce(IV)) apresenta a estrutura cristalina do tipo fluorita e o Ce_2O_3 (estado de oxidação Ce(III)) apresenta a estrutura cristalina hexagonal. Em um trabalho prévio do grupo, foi mostrada a possibilidade de controlar a área superficial, diâmetro médio e população de vacâncias de oxigênio das nanopartículas de CeO_{2-x} por meio da síntese. Além disso, as nanopartículas de óxido de cério sintetizadas apresentaram alta redutibilidade (altos valores para fração de Ce(III)) em comparação com nanopartículas de óxido de cério semelhantes existentes na literatura. A reação de redução é rotineiramente utilizada para ativar catalisadores e, em alguns casos, induz uma transição de fase com consequente alteração nas propriedades cataliticas. O principal objetivo da dissertação de mestrado foi elucidar a cinética da reação redox de nanopartículas de CeO_{2-x} altamente redutíveis.

A cinética da reação redox de nanopartículas de CeO_{2-x} com pequenos valores de x foi sondada por medidas de XRD *in situ* em atmosfera de CO em uma temperatura máxima de 900 ºC. As medidas mostraram a presença de um nova estrutura cristalina à 900 ºC, a estrutura cúbica do tipo Cu_2Se. Durante o processo de resfriamento em atmosfera de He, essa fase torna-se metaestável e transforma-se na fase fluorita devido à alta taxa de resfriamento aplicada, 15 ºC/min. A fase metaestável apresenta um coeficiente de expansão térmica negativo (α) para a faixa de temperatura de 580 ºC à 300 ºC. Usando uma aproximação da teoria de Avrami para processos não isotérmicos, a cinética de transição de fase foi estudada. Foi observado que a transição de fase ocorre em 1D com o mecanismo de cristalização controlado por difusão de volume. Portanto, a formação da fase fluorita durante o processo de resfriamento se deve à difusão de átomos de O da estrutura cristalina do tipo Cu_2Se para a fase fluorita, o que explica o valor negativo de α.

A cinética da reação redox de nanopartículas de CeO_{2-x} com altos valores de x foi investigada por medidas de XAS in situ na borda L_3 do Ce (5723 eV). Medidas de XANES in situ resolvidas no tempo para faixas de temperatura entre 900 ºC e 1020 ºC em atmosfera de CO foram conduzidas. Durante o aquecimento em atmosfera de He até a temperatura selecionada, as nanopartículas sintetizadas apresentaram um comportamento inesperado de oxidação à 450 ºC que está associado à formação da estrutura critalina triclínica. Após, na temperatura selecionada, observou-se que o tamanho médio das nanopartículas e a estrutura

cristalina desempenham um papel fundamental para elucidar o comportamento cinético, influenciando no mecanismo de redução. Em geral, as nanopartículas de CeO_{2-x} quase totalmente reduzidas apresentam o mecanismo de redução D3 que muda para o mecanismo R2 para um determinado valor da fração de Ce(III). Os mecanismos D3 e R2 estão associados às fases ricas nas estruturas cristalinas bcc e hexagonal, respectivamente. A exceção é o caso de nanopartículas com grande tamanho médio (> 50 nm) que apresentam o mecanismo R3 independentemente da fração de Ce(III). Pela primeira vez foi obtida a energia de ativação da reação de redução referente à fase bcc do óxido de cério. Os valores são muito mais elevados do que os normalmente encontrados para a fase fluorita do óxido de cério. Medidas de EXAFS *in situ* em atmosfera de CO à 500 ºC confirmam a formação da fase triclínica e a ordem atômica local em torno dos átomos de Ce depende principalmente dos parâmetros de síntese.

CONTENTS

LIST OF FIGURES

LIST OF TABLES

.

Chapter 1. INTRODUCTION

The cerium oxide CeO_{2-x} ($0 < x < 0.5$) has been studied in the last past decades due to the high technological potential in many different fields such as electrochemical devices, catalysts, hybrid solar cells, among others [1-6]. Since 1976, according to Google Scholar database, the number of publications involving the term "CeO_2" exceeds 90000 and shows an expressive increase over the years. The main characteristic that makes CeO_{2-x} a material of high current interest, especially in catalysis, is the great ability to store and release O atoms (oxygen storage capacity – OSC) which is directly related to the facility on changing the oxidation state between Ce(III) ($x = 0.5$) and Ce(IV) ($x = 0$). This characteristic makes highly reducible CeO_{2-x} widely used as an active support of catalysts, which is typically composed of transition metal nanoparticles supported on metal oxides.

The catalytic reaction typically occurs at high temperatures (T > 500 °C). It means the properties of the catalysts may be significantly altered in comparison to the room temperature case, especially for nanocatalysts. Furthermore, the reduction reaction is a fundamental step in any catalytic process because it is used to activate the catalyst. The reduction process, in the case of highly reducible CeO_{2-x}, implies on the formation of O vacancies, which are catalytically active sites for various reactions. Consequently, it is possible to occur phase transitions that influence on the catalytic properties. The main goal of this Masters dissertation was to elucidate the kinetics of redox reaction of highly reducible CeO_{2-x} nanoparticles, thereby obtaining fundamental properties for future applications.

Chapter 2 of this Master dissertation is dedicated to present a review on the main properties of cerium oxide. Chapter 3 covers the description of the physical phenomena behind the experimental techniques used. Chapter 4 presents the methodology used, results and discussion. Finally, chapter 5 is dedicated to show the conclusion and perspectives for the continuation of the project.

Chapter 2. THE MAIN PROPERTIES OF CERIUM OXIDE

This chapter aims to present the basic properties of cerium oxide and its reduction kinetics.

2.1 Cerium oxide

Cerium oxide (CeO_{2-x} ($0 \leq x \leq 0.5$)) is a ceramic material that changes the oxidation state between the fully oxidized case (Ce(IV) with $x = 0$, CeO_2) and the fully reduced case (Ce(III) with $x = 0.5$, Ce_2O_3) [1]. The CeO_2 presents a pale-yellow color and the reduction of the oxide (increase of x value) changes the color to blue, black, olive green and, finally, to mustard in the case of Ce_2O_3. Table 1 shows some important physical properties of CeO_2.

Properties	**Values**
Density	7.22 g/cm^3
Melting point	2750 K
Specific heat	460 J/ (kg K)
Thermal conductivity	12 W/ (m K)
Linear expansion coefficient	$(11.5 \pm 0.5) .10^{-6}$ /K (25 to 500) °C $(12.1 \pm 0.5) .10^{-6}$ /K (500 to 1000) °C

Table 1 – Main physical properties of CeO_2 [1].

The cerium oxide at NTP (Normal Temperature and Pressure), CeO_2, presents the fluorite-like crystal structure with a face centered cubic (fcc) unit cell, space group Fm-3m and lattice parameter a = 5.411 Å. In this crystal structure, the O anions are coordinated around 4 Ce cations positioned at the corners and centers of the cube faces forming a tetrahedron, as shown in Figure 1. The fully reduced case, Ce_2O_3, presents the hexagonal crystal structure with space group P-3m1 [7]. In this atomic arrangement the Ce atoms present the coordination number 7, with 6 O atoms forming an octahedral rearrangement around the Ce atom and another O positioned above the face of the octahedron. The facility to change the oxidation state between Ce(IV) and Ce(III) allows cerium oxide presenting a good O storage capacity. It means cerium oxide acts as O buffer under O-rich environments and it releases O atoms under reducing environments [2]. This property has positively influenced on the activities of catalysts/electrolytes in automobile emission treatment systems and solid oxide fuel cells. The

CeO_{2-x} presents intrinsic defects of O vacancies in the crystal structure, which induces the stoichiometry changes from CeO_2 to CeO_{2-x} ($0 < x < 0.5$).

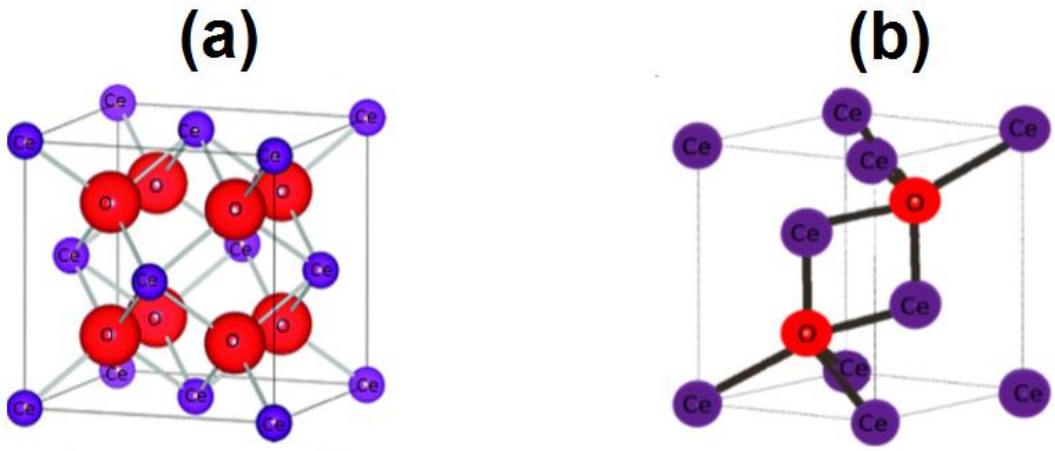

Figure 1 - Schematic representation of the unit cell of (a) CeO_2 and (b) Ce_2O_3. The O and Ce atoms are represented in red and purple, respectively. Adapted from [8] and [9].

Dae-Joon Kim [10] developed an equation relating the *x* value (proportional to the Ce(III) fraction) with the lattice parameter a of cerium oxide in the fluorite phase

$$a = (0.541 + 200x \text{ x } 2.74010 \text{ x } 10^{-4})nm \qquad (2.3)$$

where 0.541 nm is the lattice parameter of CeO_2 at room temperature, and 2.74010 x 10^{-4} is the Vegard's parameter. This equation shows the lattice parameter is directly proportional to the O vacancy population and there is an expansion in the lattice parameter by increasing the *x* value. Therefore, the reduction of CeO_2 implies in a lattice expansion even if the reaction occurs at a constant temperature.

The phase diagram relating the *x* value with the crystal structure of bulk cerium oxide at 1 atm is shown in Figure 2 [11]. This diagram shows that the possible crystal structures of cerium oxide are the fluorite (F), body centered cubic (C), triclinic (T), rhombohedra (R), and hexagonal (A) [12-13]. It is possible to observe that the presence of a given crystal structure depends closely on the temperature. At high temperatures, 900 °C < T < 1050°C, the cerium oxide presents only the F phase for $1.75 < 2\text{-}x < 2.0$ but a mix of other phases for $1.5 < 2\text{-}x < 1.75$ In special, for temperatures below 630 °C and with $1.77 < 2\text{-}x < 1.81$ there are several disordered phases not yet fully characterized but possibly presenting the triclinic symmetry. It is important to observe that a single hexagonal phase appears only for 2-*x* close to 1.5 and T >

613 °C. Moreover, this phase diagram is valid for bulk materials, which is not necessarily valid for nanoparticles. For example, Kim [14] developed the nano-phase diagram for the CeO_2-CoO system using the CALPHAD method [15]. This nano-phase diagram showed a direct dependence of the phase equilibrium curves with the nanoparticle's radius.

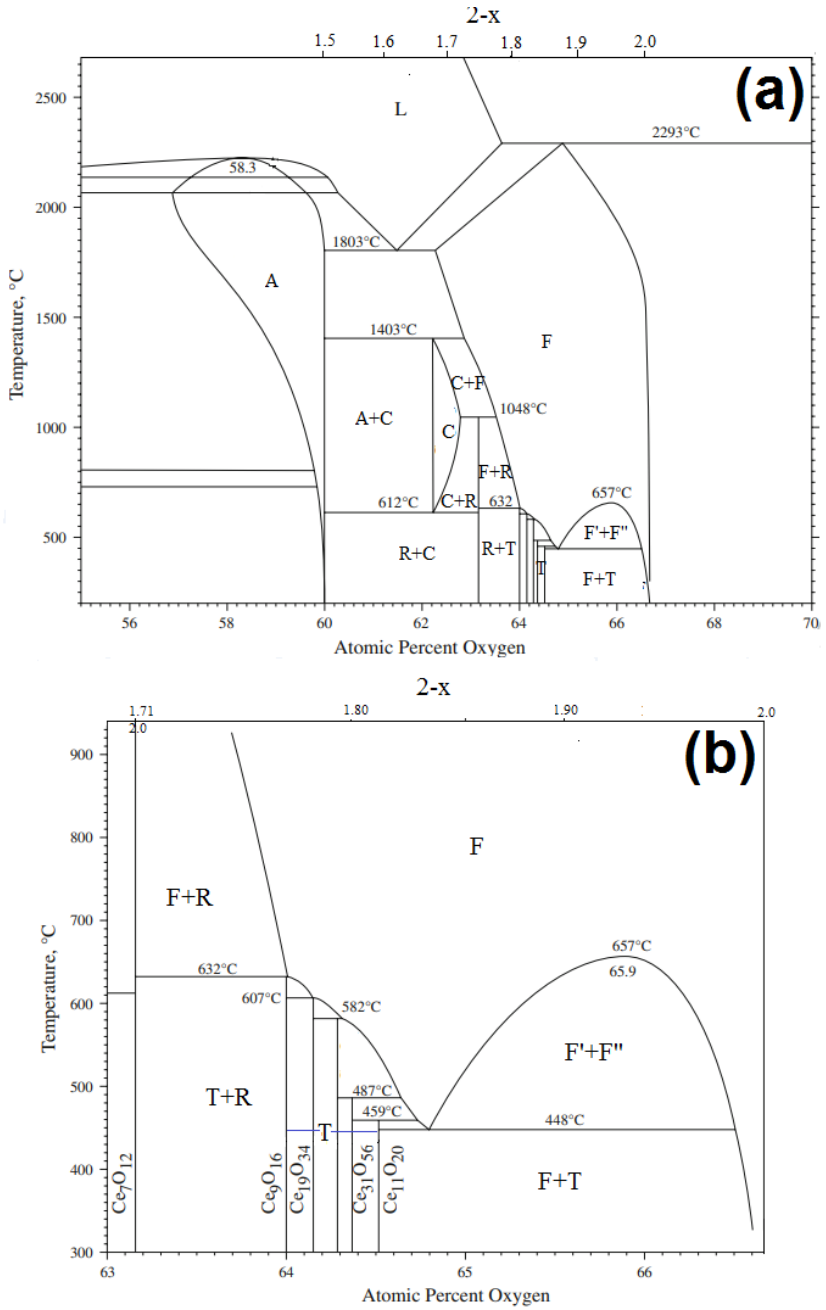

Figure 2 - Phase diagram of CeO_{2-x} at 1 atm for atomic percent oxygen from (a) 55 to 70 and (b) from 63 to 66.6. F, F', F'' stands for disordered fluorite phases with different percentages of oxygen and T, R, C, A stands for triclinic, rhombohedra, body centered cubic (bcc) and hexagonal phases, respectively. Adapted from [11].

Recently, Bekheet et al [16] investigated the reduction of micrometric cerium oxide particles exposed to a H_2 atmosphere using the in situ XRD technique. The authors heated the sample from room temperature to 1000 ºC in O_2 atmosphere, then started the reduction treatment under H_2 atmosphere. This reduction treatment allowed the presence of a bcc crystal structure. After this, the sample was cooled under H_2 atmosphere. The crystal structures formed during the cooling process are shown in Figure 3 . It is possible to observe that around 630 °C and 500 °C there is a phase transition to rhombohedral (red points) and triclinic (blue points) phases, respectively. It is important to observe that these phases are stable at room temperature but the exposition to the atmosphere oxidizes the sample, then turning to the fluorite phase. CeO_{2-x} nanoparticles are increasingly being used in catalysis [2]. However, for the best of our knowledge, there are no study in the literature dedicated on investigating the phase transition of CeO_{2-x} nanoparticles or showing the nano-phase diagram for the Ce-O system.

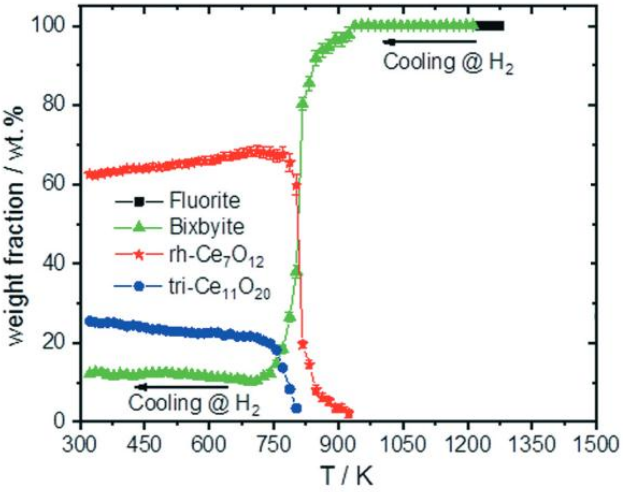

Figure 3 - Temperature evolution of weight fraction of different phases formed during cooling of CeO_2 from 1273 K to 300 K in H_2 atmospheres [16].

In a previous work of the group [17], Della Mea et al synthesized cerium oxide nanoparticles and changed some synthesis parameters like type and amount of solvent and temperature, then obtaining nanoparticles with different electronic and structural properties. It was possible to tune the O vacancy population through the synthesis procedure, which is highly desirable for catalytic applications since O vacancies represent the most important catalytically active site in cerium oxide. The nanoparticles were characterized using ex situ TEM

(Transmission Electron Microscopy), N_2 Adsorption Isotherm, XRD (X-ray Diffraction), and SEM (Scanning Electron Microscopy), and in situ time-resolved XANES (X-ray Absorption Near Edge Structure) at Ce L_3 edge and NAP-XPS (Near Ambient Pressure X-ray Photoelectron Spectroscopy) techniques during reduction treatment. The reduction treatment consisted on exposing the nanoparticles to a CO atmosphere and heating from room temperature to 500 °C. The measurements showed the high reducibility of the cerium oxide nanoparticles synthesized in comparison to the literature results. The nanoparticles reached a Ce(III) fraction of 0.92 at a low temperature of 500 ^oC. It was observed also a great change on the reduction temperature (T_R) of cerium oxide and the final Ce(III) fraction values reached at 500 ^oC, depending on the synthesis parameters. The reduction temperature reached values as low as 108 ^oC. For comparison purposes, the commercial standard did not show a significant reduction up to 500 ^oC in the same experimental conditions. Besides high surface area, small pore volume, small size and high initial Ce(III) fraction, nanoparticles with OH-free surfaces presented an improved reduction property, then decreasing the T_R value. In catalysis, the activation of catalysts is traditionally accomplished by a reduction treatment. Considering the high Ce(III) fraction values obtained, these nanoparticles should present a phase transition during the activation treatment or even during the catalytic reaction at high temperatures. Since some catalytic properties like activation energy depend on the crystal structure of the catalyst, a detailed study about the reduction kinetics in these nanoparticles is needed for future applications.

2.2 Phase transition theory

2.2.1 The Kolmogorov Johnson Mehl Avrami (KJMA) model

The KJMA [18-20] model was one of the first mathematical models describing the kinetics of phase transition and it is still used nowadays. The model is based on the following assumptions:

- The new phase is nucleated by tiny “germ nuclei” which already exist in the old phase and whose effective number N_e per unit nucleation region can be changed by the temperature. The nucleation occurs randomly and homogeneously distributed over the full non-transformed portion of the material.

- The growth rate of each nucleus does not depend on the extend transformation.
- The growth of each nucleus occurs at the same rate in all directions.

The phase transition starts with the formation of germ nuclei in the old phase. Let N(t) the number of germ nuclei as a function of time. The nuclei start to growth and N(t) decreases from the initial value (N_e) in two different ways: (i) some nuclei become active growth nuclei, N'(t), therefore these nuclei are no longer germ nuclei. The N'(t) depends on the N_e value and on the probability for the formation of growth nuclei per germ nucleus, p(T), which is essentially a function of the temperature [18]; (ii) the germ nuclei can be swallowed by growing grains of the new phase, whose number is defined as N''(t). Basically, this number depends on the volume of the new phase (V) and N_e. Therefore:

$$\dot{N} = -\dot{N}' - \dot{N}'' \tag{2.1}$$

Considering p(T) is relativity large such that almost all the nuclei start growing before any ingestion, it is possible to neglect the second term, then arriving at

$$\dot{N} = -\dot{N} = -pN \tag{2.2}$$

For isothermal processes p is constant with time [21]. By integrating both sides of equation 2.2, N becomes:

$$N = N_e e^{-pt} \tag{2.3}$$

Replacing N in (2.2) by (2.3) it is possible to obtain the number of growth nuclei at a given time t

$$N' = \int_0^t pNdt = Ne(1 - e^{-pt}) \tag{2.4}$$

Let's consider an aggregate of grains of various shapes and sizes because of the growth from different centers starting at different instants. Suppose that the growth is stopped when two grains collide each other. Then, the extension volume is defined as the grain volume before collision with another grain. Therefore, the expected total volume at time t is the total transformed volume if the overlapping of growing grains is neglected. Let V_1' be defined as the total transformed volume of non-overlapping regions of the extended volume, as indicate in Figure 4 by dotted areas. V_2' is defined as the transformed volume lying solely in double grains

regions, which is shown in Figure 4 as the single hatched areas, V_3' is defined as the triple grain regions and is shown as doubly hatched areas and son on. The total transformed volume is equal to:

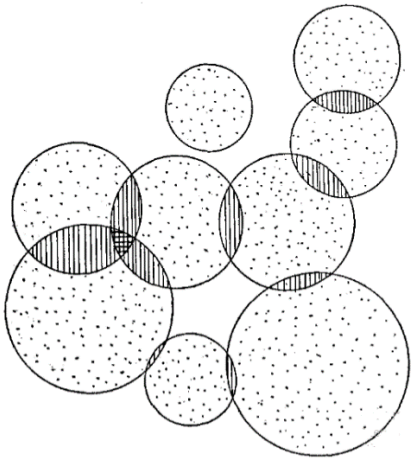

Figure 4 - Schematic representation of active growth nuclei. The dotted, singly hatched and doubly hatched areas correspond to V_1', V_2' and V_3', respectively [18].

$$V = V_1' + V_2' + V_3' + \cdots \ldots V_m' + \ldots \tag{2.5}$$

It is possible to relate the general volume extended, $V_k ex$ with V_m' and therefore with the total volume transformed by

$$V_k ex = \sum_{m=k}^{\infty} C_{k^m} V_m' \tag{2.6}$$

For example, $V_1 ex$ and $V_2 ex$ are

$$V_1 ex = V_1' + 2V_2' + 3V_3' + \cdots \ldots mV_m' + \ldots \tag{2.7}$$

$$V_2 ex = V_2' + 3V_3' + \ldots \ldots \ldots + \frac{m(m-1)}{2} V_{m'} \tag{2.8}$$

The comparison between expressions (2.7) and (2.8) with (2.5) shows that is possible to obtain the total volume transformed as a function of the extend volume using

$$V = \sum_k (-1)^{k+1} V_k ex \tag{2.9}$$

Since the total volume transformed as a function of extend volume was obtained, it is necessary to relate the extend volume with the volume of each grain v and the nucleation, N. Let G be defined as the average rate of grain growth with radius r. In general, G depends on the temperature and grain concentration. Then the grain radius r at an ordinary time t, and starting growing up at t = s, is given by

$$r(t,s) = \int_s^t G\,dx \tag{2.10}$$

Aiming to simplify the analysis, it is introduced the characteristic time scale of the substance and process, τ. This parameter represents the time needed for the number of growth nuclei becoming constant and it depends on the p(T) as p(T)dt = dτ. In this way, the grain radius depends on the characteristics of the material. Therefore, the grain radius is

$$r(\tau,z) = \int_z^\tau \frac{G}{p(T)}\,du \tag{2.11}$$

Defining G/p(T) as ε, the grain radius is

$$r(\tau,z) = \int_z^\tau \varepsilon\,du \tag{2.12}$$

Therefore, the grain volume is

$$v(\tau,z) = c\left[\int_z^\tau \varepsilon\,du\right]^d \tag{2.13}$$

where c is the shape factor and d is the dimension of the crystal growth. For isothermal processes, α is constant over the time, therefore the grain volume is

$$v(\tau,z) = c\varepsilon^d(\tau - z)^d \tag{2.14}$$

Now it is possible to define the extension volume as a function of equation (2.14) and (2.3). V_1ex at time z, the volume of each grain multiplied by the number of grains, becomes:

$$V_1ex = \int_0^\tau c\varepsilon^d(\tau - z)^d N_e e^{-pz}\,dz \tag{2.15}$$

The generalization for obtaining V_mex is more complex becauseV_2ex and V_3ex include overlapping regions and it will not be deduced here. Basically, it is necessary to calculate the

average of overlapping volume multiplied by the number of overlapping nuclei. The resulting equation is [18].

$$V_m ex = \int_0^{\tau} N(z_1)\ dz_1 \int_0^{z} N(z_2) dz_2\ \ldots\ldots \int_0^{z_m - 1} N(z_m)\ \overline{v_m} dz_m \tag{2.16}$$

where $z_1 > z_2 > z_3$ …..z_m. Therefore, using equation (2.16) in (2.9) allows obtaining the total volume transformed as a function of the material properties. However, it would require high processing power to calculate numerically these integrals. Alternatively, it is possible to use the Austin-Rickett principle [19] that establishes that "in average, the ratio of non-overlapped volume V_1' to extended volume V_1ex of a randomly selected region is equal to the density of untransformed matter (1-V)". Therefore, the following equation results

$$\frac{dV}{dV_{1ex}} = 1 - V \tag{2.17}$$

Integrating both sides and rearranging the terms gives

$$V = 1 - e^{-V_{1ex}} \tag{2.18}$$

Replacing V_1ex by (2.15),

$$V = 1 - e^{\int_0^{\tau} c\varepsilon^d (\tau - z)^d N_e e^{-pz}\ dz} \tag{2.18}$$

The result of the integral depends on the dimension of the occurrence of phase transition but the general result is

$$V = 1 - e^{-Kt^n} \tag{2.19}$$

Equation (2.19) is known as Avrami's equation for isothermal process. It is also known as

$$y(t) = 1 - e^{-Kt^n} \tag{2.20}$$

where y is the fraction of the transformed phase. The Avrami's coefficient, n, is associated to the dimension of the crystalline growth and the mechanism of phase transition and K is the crystallization rate. Tables 2 and 3 show the possible values for the Avrami's coefficient considering different a value. The constant a, related to the nucleation process, can also assume different values of 0 or 1. For a values between 0 and 1, the nucleation rate decreases with time and for a values higher than 1 the nucleation rate increases with time [22**]**. Whether there is more than one type of crystalline growth is necessary to make some assumptions about the

nucleation or the mechanism process. The use of in-situ XRD measurements allows obtaining the information about the physical mechanism of phase transition using the Avrami's theory by determining the fraction of each phase as a function of time and, consequently, the Avrami's coefficient by Equation (2.20).

Dimension of crystal growth (d)	**Mechanism of crystal growth (b)**	**Avrami's constant n = a + bd**
1	½	3/2
	1	2
2	½	2
	1	3
3	½	5/2
	1	4

Table 2 - Avrami's coefficient values for the different types of mechanism and growth dimension nucleation rate constant a = 1.

Dimension of crystalline growth (d)	**Mechanism of crystalline growth (b)**	**Avrami constant n = a + bd**
1	½	1/2
	1	1
2	½	1
	1	2
3	½	3/2
	1	3

Table 3 Avrami's coefficient values for the different types of mechanism and growth dimension nucleation rate constant a = 0.

2.2.2 The Jeziorny-modified Avrami's model

The Jeziorny-modifed Avrami's model is a first approximation of the Avrami's equation that can be used for non-isothermal processes occurring with constant cooling or heating rates

[23]. This extension of the Avrami's equation for non-isothermal processes is valid assuming that the crystallization process occurs for a fixed temperature [24]. In other words, the crystallization temperature is constant in the Avrami's equation. The single modification in the Avrami's equation is related to the crystallization rate, K, that is corrected by the crystallization parameter Kc for non-isothermal process using the following equation:

$$ln(Kc) = \frac{ln(K)}{|\varphi|} \tag{2.21}$$

where K is the crystallization rate obtained from Avrami's equation and φ is the constant cooling or heating rate. Therefore, it is still possible to determine the physical mechanism of phase transition once the heating or cooling rate is known.

2.3 Models for solid state reaction kinetics

2.3.1 General model

The reaction rate of any solid-state reaction can be described by [25]:

$$\frac{d\alpha}{dt} = Ae^{\frac{-Ea}{RT}} f(\alpha) \tag{2.30}$$

where A is a constant named pre-exponential factor, E_a is the activation energy of the reaction, T is the absolute temperature, R is the gas constant, f(α) is a function that describes the reaction model and α is the conversion fraction of the reaction, which varies between 0 and 1 with 0 representing the beginning and 1, the end of the reaction. For isothermal processes, Equation (2.30) can be easily integrated over time becoming

$$\int \frac{d\alpha}{f(\alpha)} = \int Ae^{\frac{-Ea}{RT}} dt = g(\alpha) = kt \tag{2.31}$$

where g(α) is the integrated form of f(α) and, therefore, the problem comes down in finding the g(α) function that represents the physical system studied. There are seven main equations describing the reaction mechanism. These equations can be divided in three distinct groups, namely diffusion-controlled (Dn), phase boundary-controlled (Rn) and order-based (Fn) reaction models. There is a systematic method to determine the mechanism controlling the reaction which was developed by Hancock and Sharp [26]. This method is based on the

Avrami's equation (2.20) and comprises a generalized equation for the kinetics of solid state chemical reactions. Hulbert [27] elucidated the relation between the Avrami's coefficient and the nucleation and growth models, as shown in Table 5. Later on, Go et al [28] modified it and reached a broader relationship between the Avrami's coefficient and the nucleation and growth models, also depicted in Table 4.

Reaction mechanism	**g(α)**	**Nature of mechanism**
One-dimensional diffusion (D1)	α^2	Diffusion process *n < 1*
Two-dimensional diffusion (D2)	$(1-\alpha)ln(1-\alpha)$	
Three-dimensional diffusion (D3 - Jander equation)	$[1-(1-\alpha)^{1/3}]^2$	
Three-dimensional diffusion (D4 - Ginstei equation)	$1-\frac{2\alpha}{3}-(1-\alpha)^{\frac{2}{3}}$	
First order reaction (F1)	$-ln(1-\alpha)$	First order *n =1*
Phase-boundary controlled (R2)	$1-(1-\alpha)^{1/2}$	Phase-boundary Controlled *1 < n < 2*
Phase-boundary controlled (R3)	$1-(1-\alpha)^{1/3}$	

Table 4 - Reaction mechanism and the corresponding algebraic expression.

The diffusion controlled mechanisms (Dn) often occur between different crystal lattices or with molecules permeating a lattice whose motion is restricted and dependent on the presence of lattices defects [25]. Basically, the diffusion process depends on the reactant concentration and the distance between reactants, namely the product layer (l). The schematic representation of the diffusion process is shown in Figure 5.

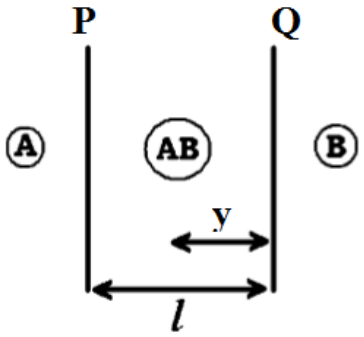

Figure 5 - Schematic representation of the diffusion-controlled mechanism in one dimension. A and B represent the reactants, AB the product interface, l the AB interface thickness, and y the distance from interface Q to AB. Adapted from [25].

For one-dimensional diffusion, the diffusion process can be represented by

$$\frac{dl}{dt} = -D\frac{M_{AB}}{M_{B\rho}}\frac{dC}{dy} \tag{2.32}$$

where dC is the differential of the concentration of reagents B, ρ is the density of the products AB and D is the diffusion coefficient. Assuming a linear concentration gradient of B,

$$l^2 = kt \tag{2.33}$$

However, the product interface thickness l is proportional to the conversion fraction of the reaction, therefore

$$\alpha^2 = k't \tag{2.33}$$

For the three-dimensional case, α is related to the mass of n spherical particles representing the product AB

$$\alpha = \frac{\frac{4}{3}n\rho\pi R^3 - \frac{4}{3}n\rho\pi(R-y)^3}{\frac{4}{3}n\rho\pi R^3} \tag{2.34}$$

As the reaction occurs, y increases until y = R when the reaction finishes. Replacing α in Equation (2.33) by Equation (2.34),

$$[1-(1-\alpha)^{1/3}]^2\, ln(1-\alpha) = k't \tag{2.34}$$

The order-based reaction models (Fn) basically consider the reaction rate proportional to the remaining reactant concentration,

$$\frac{d\alpha}{dt} = k(1-\alpha)^n \tag{2.35}$$

Considering n = 1 and integrating both sides of Equation (2.35) is obtained the F1 model shown in Table 5. This model was used for describing the reduction and oxidation mechanisms of cerium oxide for the fluorite phase, as described later on in this chapter [29].

The phase boundary-controlled model, or the geometrical contraction model, assumes that the nucleation process occurs rapidly at the crystal surface and the degradation rate is controlled by the resulting reaction interface progressing towards the center of the crystal [25], then

$$r = r_0 - kt \tag{2.36}$$

where r_0 and r are the initial radius of the particle and the radius after a given time t from the beginning of the reaction, respectively. Thus, the reaction accounts for a contraction in the reactant particles. Using the same idea of the diffusion-controlled model to describe α (Equation (2.34)) and considering equation (2.36) for n spherical particles (R3),

$$\alpha = \frac{\frac{4}{3}n\rho\pi {r_0}^3 - \frac{4}{3}n\rho\pi(r_0 - kt)^3}{\frac{4}{3}n\rho\pi {r_0}^3} \tag{2.37}$$

Rearranging the terms, it is possible to obtain the R3 model shown in Table 5

$$1-(1-\alpha)^{\frac{1}{3}} = kt \tag{2.38}$$

The three reaction mechanisms (Dn, Fn and Dn) are schematically represented in Figure 6. The lime green represents the unreacted zone and the spring green represents the reacted zone. The diffusion models consider that the crystallization rate is controlled by the transport of reactants and products to and from the active interface. The reaction order-based models assume a homogeneous reaction process in the full region. Finally, the geometrical contraction models are basically the classical shrinking core model with phase-boundary reaction control of different geometries [30].

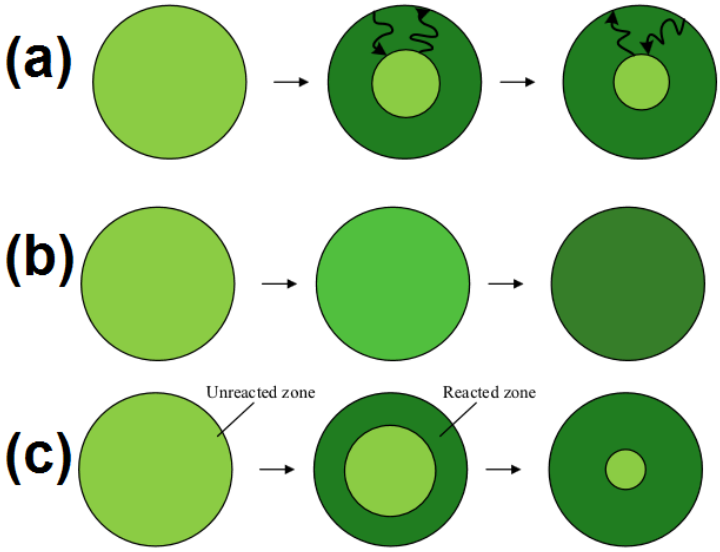

Figure 6 – Schematic representation of (a) diffusion model (Dn), (b) reaction order model (Fn) and (c) geometrical contraction model (Rn). Adapted from [30].

2.3.2 Analytical model for cerium oxide redox reactions

Bulfin et al [29] developed an analytical model to describe the redox reaction kinetics of CeO_{2-x}. This model is valid exclusively for the fluorite crystal structure. The reduction of cerium oxide can be described by

$$CeO_2 \rightarrow CeO_{2-x} + \frac{x}{2}O_2 \tag{2.23}$$

The reduction reaction depends on the O concentration ($[O_{Ce}]$), and the oxidation reaction depends on the O vacancies ($[O_{vac}]$) and O gas ($[O_{gas}]$) concentrations. Therefore, the time rate of change in the O vacancy concentration is the difference between the O leaving cerium oxide (reduction) rate and the O recombination rate (oxidation). Assuming that the reduction reaction is a first order reaction, that is, $[O_{Ce}]$ is directly proportional to the time rate of change in $[O_{Ce}]$, besides assuming that the oxidation parameter depends on $[O_{vac}]$ in first order and on $[O_{gas}]$ in nth order,

$$\frac{d[O_{vac}]}{dt} = [O_{Ce}]k_{red} - [O_{vac}][O_{gas}]^n k_{ox} \tag{2.24}$$

where k_{red} and k_{ox} are the reduction and oxidation reaction rates, respectively, and these constants follow the Arrhenius' equation

$$k_a = A_a e^{\frac{-E_a}{RT}} \tag{2.25}$$

where E_a is the activation energy of the reduction or oxidation process, R is the constant of ideal gases and A_a is a constant associated to the reduction or oxidation process. Considering this in (2.24),

$$\frac{1}{[Ce]}\frac{d[O_{vac}]}{dt} = \frac{[O_{Ce}]}{[Ce]}k_{red} - \frac{[O_{vac}]}{[Ce]}[O_{gas}]^n k_{ox} \tag{2.26}$$

$$\frac{[O_{Ce}]}{[Ce]} = \delta - x \tag{2.27}$$

$$\frac{[O_{vac}]}{[Ce]} = x \tag{2.28}$$

where (δ, x) are the stoichiometric parameters. In equilibrium, equation (2.26) can be equated to 0 and considering $[O_{gas}]$ proportional to the pressure of the O_2 gas ($P^n{}_{O_2}$),

$$\ln\left(\frac{x}{\delta - x}\right) = \frac{-\Delta E}{RT} + \ln\left(\frac{P^n{}_{O_2} A_{red}}{A_{ox}}\right) \tag{2.29}$$

where A_{red} and A_{ox} are constants associated to the reduction and oxidation processes, respectively, and ΔE is the difference between the Ea of the reduction and oxidation processes. In accordance to the literature [11], the δ value is 0.35 because it is expected that the fluorite phase is no longer stable at high temperatures (1000 – 2000°C) for $x > 0.35$ and thus a phase transition occurs. Therefore, the Bulfin's equation equals to

$$\ln\left(\frac{x}{0.35 - x}\right) = \frac{-\Delta E}{RT} + \ln\left(\frac{P^n{}_{O_2} A_{red}}{A_{ox}}\right) \tag{2.29}$$

Therefore, it is possible to obtain the ΔE value of reduction and oxidation processes of cerium oxide through the determination of x for different temperature values. The main limitation of the method is the applicability for the redox processes of barely the fluorite phase.

This Master dissertation is dedicated to elucidate the kinetics of the redox reaction of highly reducible CeO_{2-x} ($0 < x < 0.5$) nanoparticles. In special, it is aimed to determine the physical mechanism and the activation energy of the redox reaction.

Chapter 3. EXPERIMENTAL TECHNIQUES

In this chapter it will be discussed the physical phenomena behind the experimental techniques used for characterization of the cerium oxide nanoparticles, X–ray Absorption Spectroscopy (XAS), X-ray Diffraction (XRD) and Transmission Electronic Microscopy (TEM). The XAS and XRD measurements were performed using synchrotron radiation, then it will be first discussed the physical principles of this kind of radiation.

3.1 Synchrotron radiation

The synchrotron radiation is the electromagnetic radiation issued by relativistic charged particles deflected by a magnetic field. Synchrotron radiation covers the electromagnetic spectrum from the infrared to the hard X-rays (high energy X-rays) region. The Synchrotron laboratories consist of a linear accelerator (Linac) that typically accelerates electrons to a final energy of few MeV. These electrons are injected into an intermediate circular accelerator, denominated booster, with the objective of increasing the electron energy to the operation energy. Posteriorly, the electron beam is injected into the storage ring, as shown in Figure 7. The electron beam presents an energy of few GeV, which represents electrons with around 99.99999% of the light speed. In the storage ring, the electrons are deflected through the application of a magnetic field perpendicular to the trajectory of the electron beam by using magnetic dipoles (bending magnet device), thus generating synchrotron radiation. The radiation is emitted tangentially to the trajectory in a narrow cone. The electron beam is kept in ultra-high vacuum, (10^{-9} – 10^{-10}) Torr, to avoid electrons losing a high amount of energy by collisions with the molecules. Nevertheless, the electron beam loses energy due to collision with residual molecules and by the emission of synchrotron radiation. For this reason, a radio frequency cavity is used to furnish energy to the electron beam after a turn. There are also insertion devices, located in the straight section of the storage ring, that are magnetic devices supplying periodic magnetic fields in order to improve the brilliance and to produce short pulses regarding frequency or time. Basically, there are two types of insertion devices: wigglers and undulators. Wiggler devices consist of a series of alternating dipole magnets, then the superposition of emitted radiation from each wiggle enhances the brilliance and it is directly proportional to the number of poles and the corresponding magnetic field strength. The construction of the

undulators are similar to the wiggler ones. However, the undulators are operated at a reduced field strength. The radiation obtained from wiggler insertion devices is polychromatic and consist of short temporal pulses while that from undulator is a quasi-monochromatic light with wide time distribution.

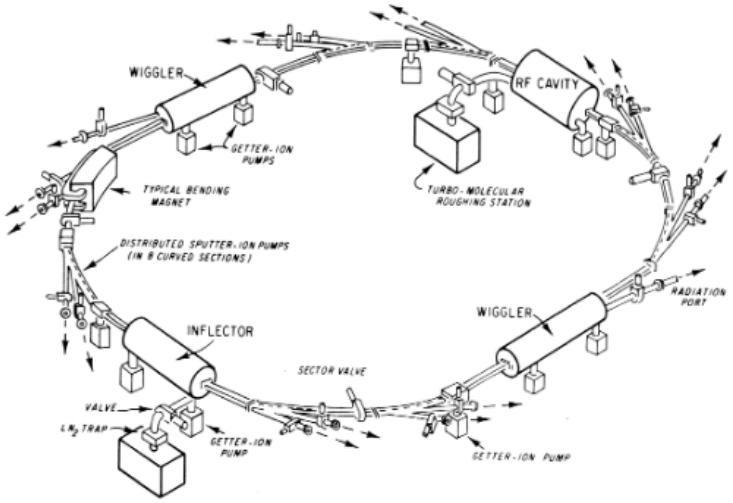

Figure 7 - Schematic representation of an intermediate energy electron storage ring designed as a source of synchrotron radiation [31].

Some advantages of the synchrotron radiation are listed below:

- **High brilliance**: the brilliance is defined as the photon flux per unit of solid angle and spectral band width. The typical brilliance of synchrotron radiation sources is thousands of times bigger than that produced by conventional X -ray tubes.
- **Short pulses**: pulses with temporal width as shorter as 1 ps, which allows time-resolved experiments.
- **Polarization**: the light polarization is tunable between linear or right and left circularly polarized.
- **Wide energy range**: the synchrotron radiation includes photons from the infrared to the hard X-ray energy region. The user can choose the energy desired for a specific application.
- **Low emittance**: the emittance is defined as the beam size multiplied by the beam divergence. It means the light beam is highly collimated, which is important for space resolved experiments.

Considering this, several techniques are available in Synchrotron radiation sources, improving the quality of the measurements in comparison to a conventional X-ray source or even allowing new experiments not available in conventional X-rays source systems.

3.2 X-ray Diffraction (XRD)

The XRD technique is a method of non-destructive analysis and corresponds to one of the main microstructural characterization techniques of crystalline materials. The physical phenomenon of the XRD technique consists on the scattering of the incident X-ray by a single atom of the crystal structure and the interference between the scattered waves by different atoms. W. L. Bragg deduced equation 3.1 of X-ray diffraction in crystal structures:

$$n\lambda = 2d_{hkl}sin\theta, n = 1, 2, 3 \ldots \quad (3.1)$$

where λ is the wavelength of the incident beam, n is an integer number, θ is the angle between the incident beam and the surface of the material and d_{hkl} is the interplanar distance, as shown in Figure 2.

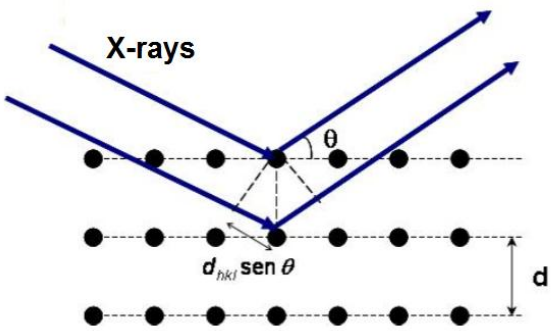

Figure 8 - Schematic representation of a X-ray beam scattered by the atoms of a given crystalline plane [32].

The Bragg's equation provides a simple model to understand the conditions required for constructive interference in the XRD measurements relating the distance between crystalline planes and the angle of the incident beam.

The XRD technique consists of measuring the X-ray intensity as a function of the 2θ value. Figure 9 shows a typical diffractogram for CeO_2 nanoparticles. It is possible to verify the existence of Bragg reflections representing constructive interference, which indicate the

presence of a crystalline material. The Bragg reflection is associated to a family of crystalline planes identified by the Miller index (hkl). In this way, indexing of the XRD pattern allows identifying the crystal structures present in the material by using databases like the Inorganic Crystal Structure Database (ICSD). A great advantage of the XRD technique is the possibility of in situ measurements since it can yield quantitative analysis to study reaction rate constants, activation energy and phase equilibria.

Furthermore, the width of the Bragg reflection is associated to the mean crystallite size and it is possible to estimate this value using the Scherer's equation [32]:

$$\tau = \frac{k\lambda}{\beta cos(\theta)} \tag{3.3}$$

where τ is the mean crystallite size, λ is the X-ray wavelength, k is the shape factor, θ is the angle of the Bragg reflection and β is the full width at half maximum (FWHM) of the Bragg reflection. The shape factor is a dimensionless quantity dependent on the crystallite shape and it is 0.89 for spherical shapes.

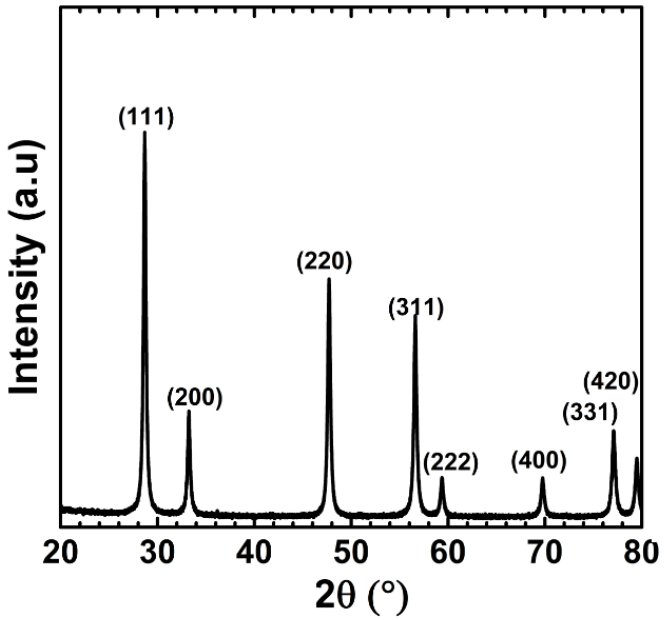

Figure 9 - Typical XRD pattern for CeO_2 nanoparticles.

The intensity of the Bragg reflection depends on 6 distinct factors [32]:

- **Form factor (f)**: it is also known as atomic scattering factor and it is defined as the ratio of the scattering amplitude by a single electron to the scattering amplitude of the atom. The XRD pattern intensity is proportional to the square of the form factor, $I \propto f^2$.
- **Structure factor (F)**: it describes how the X-ray beam is scattered by the atoms in a given crystal structure. The structure factor is obtained mathematically by:

$$F_{\Delta k} = \sum_j f_j e^{-i\Delta\vec{k}.\vec{r_j}} \tag{3.4}$$

where $\vec{r_j}$ is the position vector of the atom j in the unit cell, f_j is the form factor referent to the atom j and $\Delta\vec{k}$ is the scattering wave vector. The XRD pattern intensity is proportional to the square of the structure factor, $I \propto F^2_{\Delta k}$

- **Multiplicity factor**: it is related to the families of planes that contribute for the same Bragg reflection. For example, the families of planes {100} of fcc crystal structure presents 6 equivalents planes that contribute to the same Bragg reflection, namely (100), (010), (001), $(\bar{1}\,00)$, $(0\bar{1}\,0)$, and $(00\bar{1}\,)$. The intensity of the Bragg reflection is proportional to the multiplicity factor (p) of the plane, $I \propto p$.
- **Absorption factor**: it depends on two parameters, the absorption coefficient of the sample and the X-ray path length (x) in the sample, which depends on the geometry of the experiment. For the Bragg-Brentano geometry, the absorption factor is independent of θ, therefore all the Bragg reflections change at the same proportion.
- **Temperature factor**: the increasing of the temperature gives an increase of the atomic vibration around the equilibrium position. It gives an increase of thermal disorder that widens the Bragg reflection, besides decreasing the intensity of the Bragg reflections. The exact dependence of the intensity of the Bragg reflection with the temperature is not trivial but the most used model accounts for an exponential dependence with $I \propto e^{-2M}$, where M is a function of temperature.
- **Lorentz polarization factor**: the Lorentz factor is a geometric correction due to the incident beam divergence and the partial beam monochromatization. This factor is given by $\frac{1}{4sin^2\theta\,cos\theta}$. The polarization factor is a correction due to the split of the X-rays in the sample into two privileged directions. This factor is given by $\frac{1+cos^2\theta}{2}$. Both factors give the Lorentz polarization factor and the intensity of the Bragg reflection is given by $I \propto \frac{1+cos^2\theta}{8sin^2\theta cos\theta}$

Considering this, the intensity of the Bragg reflection is proportional to the following expression:

$$I \propto |F_{\Delta k}|^2 p \frac{1+cos^2\theta}{8sin^2\theta cos\theta} e^{-2M} \quad (3.4)$$

Aiming to perform a quantitative analysis of the diffractograms, the Rietveld refinement method is the most used one.

3.2.1 Rietveld refinement method

The Rietveld Refinement method consists on adjusting a theoretical curve to the experimental diffractogram by using the square minimum method to minimize the difference between the theoretical and the experimental curve. The method considers that the best fit of a set of N values obtained experimentally (y_i^E) by a function model $y_i^T(a,2\theta_i)$, which depends on M refined parameters a, is achieved when a minimum value of χ^2 is obtained. The χ^2 is defined as:

$$\chi^2 = \sum_i \frac{|\, y_i{}^E - y_i{}^T(a, 2\theta_i)|^2}{\sigma_i{}^2} \quad (3.6)$$

where σ_i^2 is the variance of the y_i^E. The y_i^T factor is given by the following expression:

$$y_i{}^T = s \sum_k [L_k |F_k|^2 \omega(2\theta_i - 2\theta_k) A_k T_k P_k] + y_i(bkg) \quad (3.7)$$

where the sum covers the Miller indexes (h k l) that contribute to the diffraction intensity. Besides this, the other variables are defined as:

s: scale factor;

L_k: term containing the Lorentz polarization factor and the multiplicity factor;

F_k: structure factor;

$2\theta_k$: central position of the Bragg reflection k;

A_k: asymmetry factor;

T_k: transmission factor;

P_k: factor describing the preferential orientation;

ω: function describing the reflection profile;

y_i(bkg): baseline at the i-th point.

Equation 3.7 describes generically how to calculate the theoretical curve of a diffraction pattern. In some cases, like in the present work, the A_k, T_k and P_k parameters are not used and therefore will not be discussed in details. For XRD measurements using synchrotron radiation, the polarization factor turns to the following expression [33]:

$$Li = \frac{1 - K + K.CTHM.\cos(2\theta_i)^2}{2sin^2\theta_i cos\theta_i} \quad (3.8)$$

where CTHM is the monochromator polarization correction, and K is a factor that depends on the polarization of the radiation used.

3.2.2 Experimental procedure

The XRD measurements can be performed in three different experimental methods: the von Laue method, rotating-crystal method and the powder method. The von Laue method consist on focusing a polychromatic beam in the sample that consists of a single crystal. The crystal selects and diffracts the discrete values of λ for which the angle θ and the interplanar distance d_{hkl} satisfy the Bragg's law (Equation 3.1). The rotating-crystal method consist on focusing a monochromatic X-ray beam in the sample that consists of a single crystal. Then, the sample is rotated around one of its axes. The X-ray beam is diffracted in a given crystalline plane during rotation. Whether the value of θ satisfies the Bragg's law there is a constructive interference in the XRD pattern. The powder method is based in to transform the sample in a fine powder with the objective to guarantee the existence of a polycrystal where the grains (single crystals) are randomly oriented. Then, a monochromatic X-ray beam is directed to the sample and the wavelength is kept constant during the measurement but the detection angle is changed. The geometry utilized in the XRD measurements of the present study is the Bragg-Brentano (θ-2θ) one, where the X-ray source is fixed, the detector moves in a circle with speed of 2θ/s and the sample moves with speed of θ/s. In this way, the radiation is focused on the sample holder with an angle θ in relation to the sample surface and the diffracted beam is detected with a 2θ angle in relation to the incident beam, as shown in Figure 10. Since the incident radiation promotes other effects, mainly fluorescence, a set of slits is added to the system to minimize influence from fluorescence effect and to ensure focusing of the diffracted

beam. Monochromators and filters are also added to monochromatize the X-ray beam and to reduce radiation from non-coherent scattering, respectively.

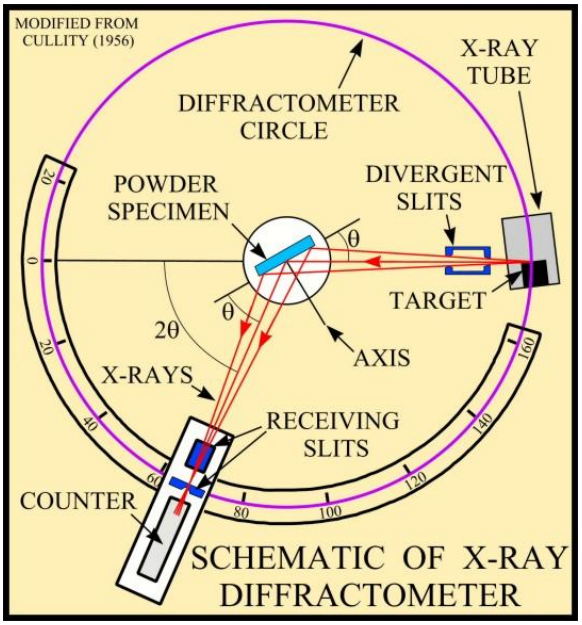

Figure 10 - Schematic representation of a X-ray diffractometer in the Bragg-Brentano geometry (θ - 2θ) [32].

3.3 X- ray Absorption Spectroscopy (XAS)

The XAS technique is used to investigate the local atomic order and the electronic structure of crystalline or amorphous materials. This technique is based on the measurement of the X-ray absorption coefficient as a function of the incident photon energy. The absorption coefficient, μ, is related to the probability of the X-ray absorption. The Beer-Lambert's law describes the relation between the incident and transmitted X-ray intensities [34]:

$$I = I_0 e^{-\mu(E)x} \tag{3.9}$$

where I_0 is the incident X-ray intensity, x is the sample's thickness, and I is the intensity transmitted through the sample. The incident photon interacts with the material according to different physical processes like photoelectric effect, Compton effect and pairs production. In the X-ray region of the electromagnetic spectrum, the effect with highest probability to be observed is the photoelectric effect, where an atom can absorb the incident photon with energy hυ and, consequently, to eject a photoelectron with kinetics energy (E_c) given by

$$E_c = E - E_b - \varphi \quad (3.10)$$

where E_b is the electronic binding energy and φ is the sample's work function (minimum energy needed to extract an electron from the surface of a solid). The photoelectric effect is the relevant physical process behind the XAS measurements.

Figure 11 shows a typical XAS spectrum measured at the Ce L_3 edge of CeO_2 nanoparticles. The spectrum corresponds to an electronic transition from 2p → 5d electronic level of the Ce atom. The sudden increase in the absorption coefficient at around 5723 eV is named absorption edge and its energy is characteristic of each electronic transition of a given chemical element. The absorption edge indicates the energy needed to induce the electronic transition. For incident photon energies higher than the absorption edge there are oscillations in the X-ray absorption coefficient, which are very useful to extract structural information. The oscillations come from the wave character of the photoelectron emitted. The wave associated to the photoelectron emitted scatters in the neighboring atoms. The backscattered wave interferes with the wave associated to the emitted photoelectron. The interference modulates the absorption coefficient, that reaches maximum and minimum values for constructive and destructive interference, respectively. The XAS spectrum can be divided in two energy regions, namely the X-ray Absorption Near Edge Structure (XANES) and Extended X-ray Absorption Fine Structure (EXAFS), as shown in Figure 11.

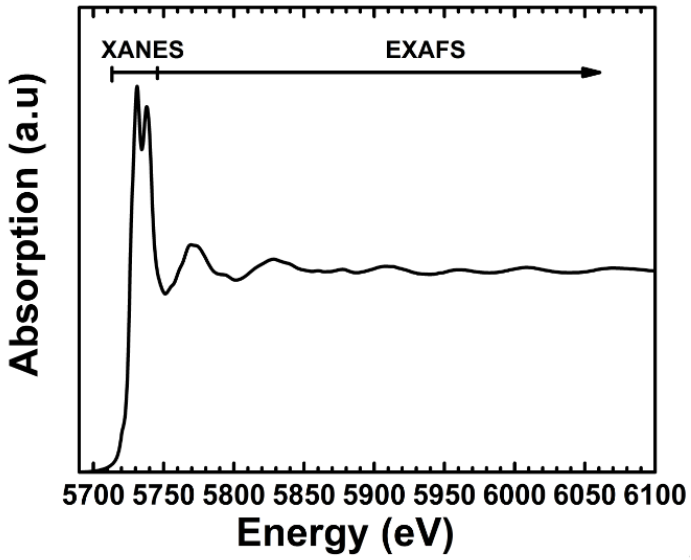

Figure 11 - XAS spectrum measured at the Ce L_3 edge of CeO_2 nanoparticles.

3.3.1 XANES

The XANES region corresponds to the energy region from the absorption edge to (50-100) eV after the absorption edge. The analysis of the XANES region provides electronic and geometrical information around a specific atom. This region is dominated by multiple photoelectron scattering events due to the small kinetics energy of the photoelectron. Considering this, the computational simulation of the XANES spectrum is not trivial due to the inherent difficulty on reproducing the real potential felt by the emitted photoelectrons. Nevertheless, it is possible to obtain quantitative information by considering different approaches:

- **Coordination chemistry**: this approach considers the type of chemical geometry that changes the format of XANES oscillations [35];
- **Molecular orbital**: it considers hybridization effects to explain changes in the absorption coefficient at the pre-edge region [36];
- **Band structure**: it is possible to obtain the relative density of holes by comparison between the height of the first maximum at the absorption edge of multiple samples [37];

The most common method used to extract quantitative information from XANES spectra is the Linear Combination Analysis (LCA). The LCA method is based on the existence of different fingerprints at the XANES spectra, which depends on the chemical state of the absorbing atom. It consists on using a linear combination of the standard XANES spectra to fit the experimental XANES spectrum (μ_e) [34]. In other words,

$$\mu_e = \sum_j \alpha_j \mu_t \tag{3.11}$$

where μ_t is the standard XANES spectrum and α_j is the fraction of this component.

3.3.2 EXAFS

The EXAFS region corresponds to the energy region from the final of the XANES until the end of the XAS spectrum, typically around 1000 eV after the absorption edge. The EXAFS region is characterized by the presence of small amplitude oscillations if compared to those present in the XANES region. The analysis of the EXAFS region allows obtaining structural information around the absorbing atom like coordination number, distance between the absorbing and scattering atoms and the Debye-Waller factor, which describes the structural and thermal disorder of the material.

The electronic transition induced by the X-ray beam is described by the Fermi's Golden rule

$$\mu(E) \propto |\langle i|\hat{\mathrm{H}}|f\rangle|^2 \tag{3.12}$$

where $\langle i|$ represents the initial state (before X-ray absorption), $|f\rangle$ represents the final state (a core hole and a photoelectron), and $\hat{\mathrm{H}}$ is the Hamiltonian operator of the interaction. The final state can be separated in two parts

$$|f\rangle = |f_0\rangle + |\Delta f\rangle \tag{3.13}$$

where $|f_0\rangle$ is the contribution of an isolated atom and $|\Delta f\rangle$ is due to the neighboring atom contribution. Then applying equation 3.13 into 3.12,

$$\mu(E) \propto |\langle i|\hat{\mathrm{H}}|f_0\rangle|^2 \left[1 + \langle i|\hat{\mathrm{H}}|\Delta f\rangle \frac{\langle f_0|\hat{\mathrm{H}}|i\rangle^*}{|\langle i|\hat{\mathrm{H}}|f_0\rangle|^2} + CC\right] \tag{3.14}$$

where CC stands for the complex conjugate. Let $\mu_0(E)$ the absorption of a hypothetic isolated atom. It is possible to demonstrate that

$$\mu(E) = \mu_0(E)[\,1 + \chi(\mathrm{E})] \tag{3.15}$$

where χ(E) is the EXAFS oscillations and it is given by

$$\chi(E) \propto \langle i|\hat{\mathrm{H}}|\Delta f\rangle \tag{3.16}$$

The Hamiltonian of the interaction between the X-ray beam and the electron is proportional to the term $\vec{p}.\vec{A}$, where $\vec{p}$ is the momentum vector and $\vec{A}$ is the vector potential, which is proportional to e^{ikr}. Considering this, the $\chi(E)$ term can be written as

$$\chi(E) \propto \int dr\, \delta(r) e^{ikr} \psi_{scatter}(r) = \psi_{scatter}(0) \tag{3.17}$$

Equation 3.17 shows that $\chi(E)$ is proportional to the amplitude of the wave function associated to the backscattered photoelectron at the absorber atom position.

It is possible to describe the wave function of the emitted photoelectron using the spherical wave function and considering this in Equation 3.17,

$$\chi(k) \propto \psi_{scatter}(k, r=0) = \frac{e^{ikR}}{kR}\left[2kf(k)e^{i\delta(k)}\right]\frac{e^{ikR}}{kR} + CC \tag{3.18}$$

where f(k) is the scattering amplitude, $\delta(k)$ is the phase shift and R is the distance traveled by the photoelectron before backscattering. Combining these terms and using the complex conjugate to make sure it ends up with a real function,

$$\chi(k) = \frac{f(k)}{kR^2}\sin[2kR + \delta(k)] \tag{3.19}$$

This equation is valid for a single pair of absorbing and scattering atoms. However, for a real measurement there are several atomic pairs to be considered. As a first approximation, the bonding environment and disorder effects change the XAFS equation from 3.19 to

$$\chi(k) = \frac{Ne^{-2k^2\sigma^2}ef(k)}{kR^2}\sin[2kR + \delta(k)] \tag{3.20}$$

where N is the coordination number and σ^2 is the Debye-Waller factor. Considering the possibility of photoelectron scattering by distinct atomic shells *j* around the absorbing atom,

$$\chi(k) = \sum_j \frac{N_j e^{-2k^2\sigma^2} f_j(k)}{kR_j{}^2} \sin\left[2kR_j + \delta_j(k)\right] \quad (3.21)$$

Equation 3.12 reproduces some of the main features behind the EXAFS measurement. However, to satisfactorily analyze the EXAFS oscillations in real systems is necessary to include additional terms ad-hoc:

- **λ(k):** It was neglected the fact that the photoelectron can also scatters inelastically from other sources like conduction electrons and phonons. Another important point to be taken into account is the core-hole lifetime, that means the scattered portion of the photoelectron wavefunction needs to be back to the absorbing atom before the excited state decays back to the core level by Auger or fluorescence processes. Then it is used a damped spherical wave function

$$\psi(k,r) = \frac{e^{ikr} e^{-r/\lambda(k)}}{kr} \quad (3.22)$$

  where λ^{-1} is equal to the sum of the inverses of the inelastic mean free path and the length associated to the finite lifetime of the hole created at the core level.

- **S_0^2, intrinsic losses**: this term accounts for the relaxation of the absorbing atom with multiple electron excitations due to the interaction with the emitted photoelectron. It is simplified by a constant multiplying Equation 3.21, where typically $0.7 < S_0^2 < 1.1$.

- **Multiple scattering of the photoelectron**: it considers that the photoelectron may scatters from more than one neighboring atom. Figure 12 shows some possible scattering paths. The inclusion of multiple scatterings is made by summing over the scattering paths instead of only the atomic shells. The R value is defined as the half path length.

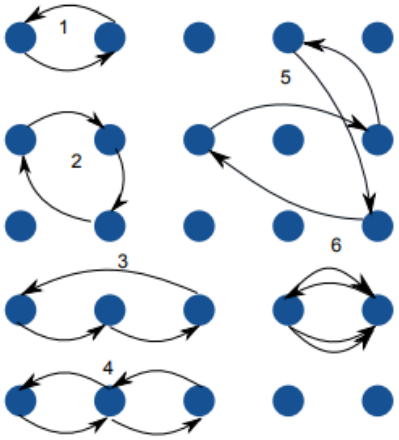

Figure 12 - Schematic representation of possible photoelectron paths (black arrows) after emission from the absorbing atom. Path 1 represents a single scattering path, 2 and 5 represent multiple scattering paths and 3, 4 and 6 represent forward multiple scattering paths [38].

Considering this, the EXAFS equation arrives to the final form

$$\chi(k) = \sum_j \frac{{S_0}^2 N_j e^{-2k^2\sigma^2} f_j(k) e^{-2R_j/\lambda(k)}}{k{R_j}^2} \sin\left[2kR_j + \delta_j(k)\right] \tag{3.23}$$

Equation 3.23 shows that the EXAFS oscillations consist of a sum of waves that correspond to the photoelectron scattering at atomic shells. For this reason, it is common to use the Fourier Transform (FT) of the EXAFS oscillations to make easier the interpretation of the data. Figure 13 shows typical EXAFS oscillations, extracted from the experimental XAS spectrum measured at Ce L_3 edge, and the corresponding Fourier Transform. The Fourier Transform represents an absorbing atom at the position R = 0 Å and each peak corresponds to a given neighboring around the absorbing atom.

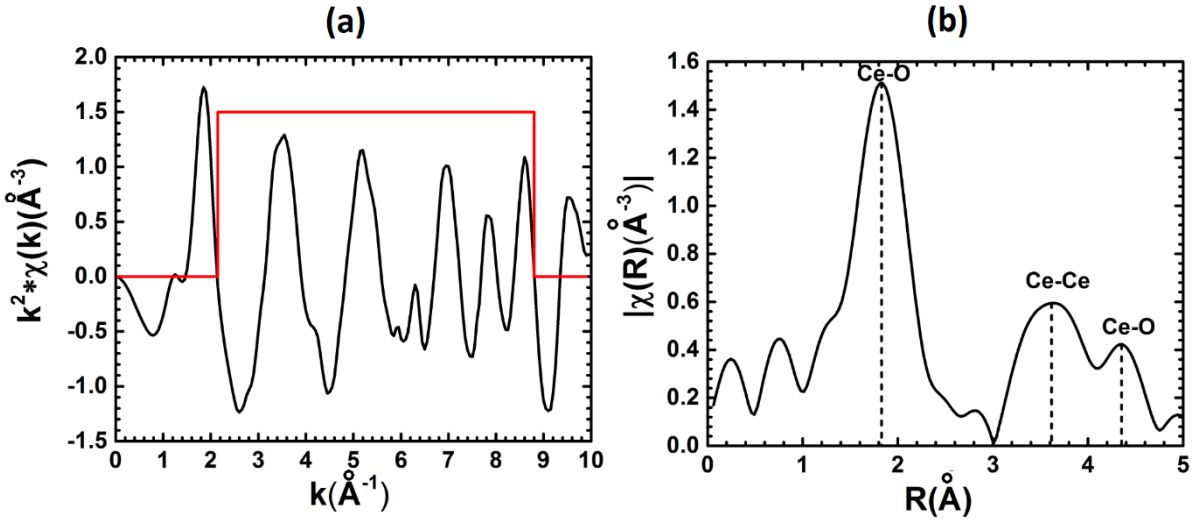

Figure 13 - (a) EXAFS oscillations and (b) the corresponding Fourier Transform measured at the Ce L_3 edge of CeO_2 nanoparticles. The red line represents the window used for the Fourier Transform.

1.3.3 Experimental method

There are three possible modes of measuring XAS spectra, namely fluorescence, total electron yield and transmission mode. The transmission mode is the most used one and will be described in more details. It is based on measuring the intensity of the incident and transmitted X-ray beam through the sample by using ionization chambers. A standard is positioned behind the sample to calibrate the incident beam energy as shown in Figure 14.

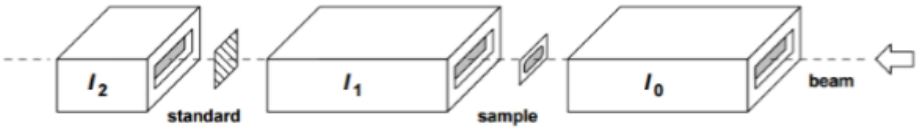

Figure 14 - Illustration of a typical experimental arrangement used in the XAS measurements in the transmission mode [39].

The ionization chamber consists of a chamber filled with a specific gas (depending on the edge probed) and two metal plates where a potential is applied. The passage of the beam induces ionization of the gas, then creating electron-hole pairs. The charges of the ionized gas

are captured by the metal plates and an electric current is measured. Since the incident X-ray beam is monochromatic and its energy is known, the electric current measured is directly related to the intensity of the X-ray beam.

The XAS measurements can also be performed in the dispersive mode, like that available at the Dispersive X-ray Absorption Spectroscopy – DXAS beamline at LNLS [40]. It consists on the incidence of a polychromatic beam in the sample instead of using the monochromatic beam of conventional XAS measurements. The polychromatic beam is achieved thanks to the presence of a curved Si crystal. The transmitted beam is detected by a CCD camera, thus allowing fast XAS measurements and consequently time-resolved XAS spectra. Figure 15 shows a schematic representation of the DXAS beamline. The great advantage of the XAS technique is the possibility to perform in situ measurements. It allows probing catalysts in real conditions, then addressing the chemical reaction kinetics.

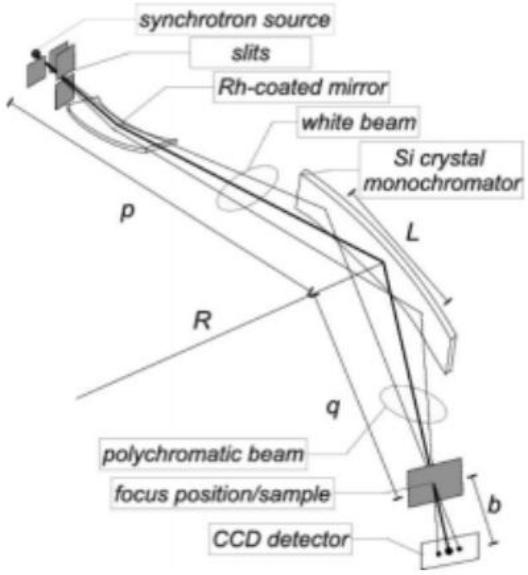

Figure 15 - Schematic representation of the DXAS beamline at LNLS [41].

3.4 Transmission Electron Microscopy (TEM)

TEM is a powerful technique able to provide information about the size, crystal structure and morphology of nanoparticles, widely applied in several research fields [42]. The working principle is analogous to the light microscope, where the main difference is the use of an electron beam instead of light to image the sample. The great advantage of using electrons is

the improved image resolution obtained because the smallest distance that the microscope can resolve is proportional to the wavelength (λ) of the incident radiation. It means the shorter the wavelength the better is the resolution. For this reason, an electron beam of 80 keV – 300 keV is used to obtain $\lambda < 1$nm, which is much smaller than the wavelength of the visible light (400 nm $< \lambda <$ 700 nm).

A transmission electron microscope can be divided in three parts: illumination system, specimen stage and imaging system as shown in Figure 16. The illumination system consists of an electron gun, acceleration column and condenser electron lenses. The electrons are generated in the electron gun, typically by the thermionic emission, and are accelerated by the presence of an electric field. The condenser lenses are used to provide a convergent beam focused at the sample position. The transmitted beam is refocused by intermediate and projector lenses that produce the final image. Finally, the magnified image is formed at the phosphorous screen.

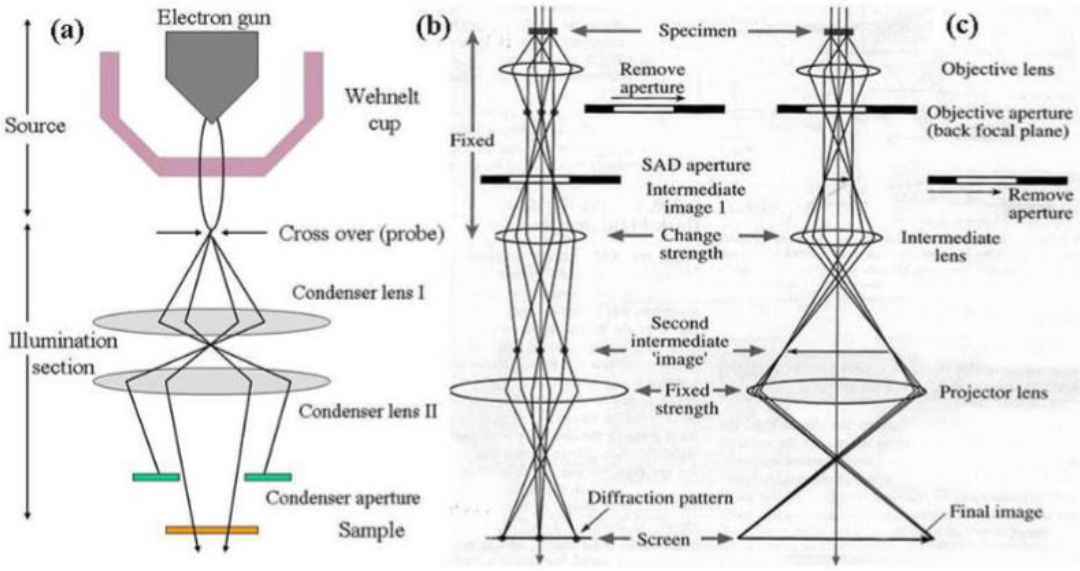

Figure 16 - A schematic representation of (a) electron source and illumination part, (b) diffraction pattern formation and (c) image formation of a transmission electron microscope [42].

It is possible to set up the microscope to obtain images with three different types of contrast: the amplitude, diffraction and phase contrasts. The amplitude contrast results from variations in the mass, thickness or a combination of both and it occurs because the cross section for elastic scattering is a function of the atomic number Z. So, it is expected the high Z regions scatter more electron than the low Z regions of the same thickness. In this case the high Z

regions would appear darker than the low Z regions in the image. Whether considering the same Z value, the thicker regions transmit less electrons than the thinner ones and it appears darker as well. Figure 17 shows a typical TEM image of CeO_2 nanoparticles where the dark regions represent the nanoparticles.

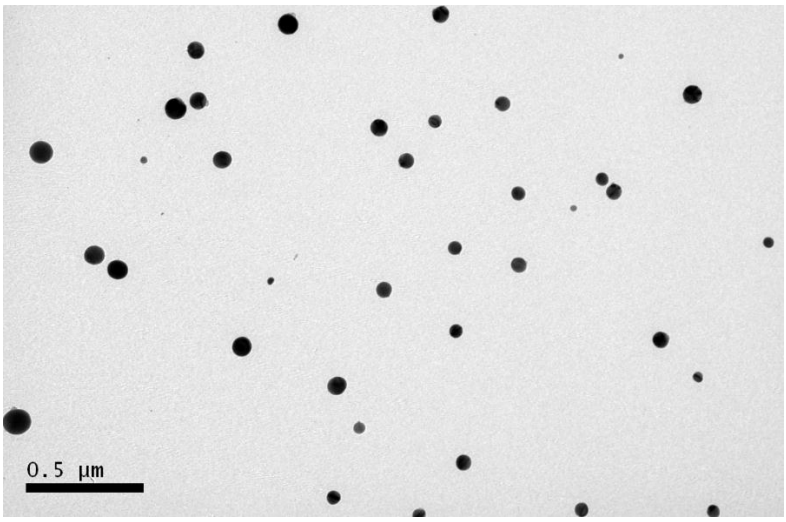

Figure 17 - Typical TEM image of CeO_2 nanoparticles.

The diffraction contrast comes from analyzing a specific Bragg reflection of the diffraction pattern produced. The diffraction patterns are obtained by choosing appropriated apertures, which allows obtaining the crystal structure of the material. The phase contrast is based on the change of the phase of the incident beam caused by the interaction with the specimen, which changes the interference pattern observed. This contrast is used in High Resolution TEM measurements.

Chapter 4. REFERENCES

[1] M. Mongensen et al, "Physical, chemial and electrochemical properties of pure and doped ceria," *Solid State Ionics,* vol. 129, no. 1-4, pp. 63-94, 2000.

[2] A. Trovarelli, "Catalytic properties of ceria and CeO_2 - contaning materials," *Catalysis Reviwes,* vol. 38, no. 4, pp. 439-520, 1996.

[3] M. Tiziano et al, "Fundamental and catalytic applications of CeO_2 - based materials," *Chemical Reviews,* vol. 116, pp. 5987- 6041, 2016.

[4] D. R. Bohn et al, "Artificial cerium-based proenzmes confined in lyotropic liquid crystals: synthetic and ond-demand activation," *Journal of Materials Chemistry B,* vol. 6, pp. 4920-4928, 2018.

[5] W. T. Figueiredo et al, "Determing the surface atomic population in Cu_xNi_{1-x}/CeO_2 ($0 < x < 1$) nanoparticles during reverse water-gas shift (RWGS) reaction," *Journal of Physical Chemistry C,* vol. 124, pp. 16868-16878, 2020.

[6] A. S. Thill et al, "Shifting the Band Gap from UV to Visible Region in Cerium Oxide Nanoparticles," *Applied Surface Science,* vol. 528, p. 14860, 2020.

[7] G. Y. Adachi, "The binary rare earth oxides," *Chemical Review,* vol. 1514, p. 1479, 1998.

[8] L. Malavasi et al, "Oxide-ion and proton conducting electrolyte materials for clean energy applications: structural and mechanistic features," *Chemical Society Reviews,* vol. 39, no. 11, pp. 4370-437, 2010.

[9] D. Taylor, "Thermal expansion data: III sesquioxides, M_2O_3, with corundum and the A-, B- and C-M_2O_3 structures," *Trans. Journal British Ceramic Society,* vol. 83, p. 92, 1984.

[10] D. J. Kim , "Lattice parameters, ionic conductivities, and solubility limits in fluorite-structure MO_2 oxide [M= Hf4*, Zr^{4+}, Ce^{4+}, Th^{4+}, U^{4+}] solid solution," *Journal of the American Ceramic Society,* vol. 72, no. 8, pp. 1415-1421, 1989.

[11] M. Zinkevich et al, "Themodynamic modelling of hte cerium-oxgen system," *Solid State Ionics,* vol. 177, no. 11-12, pp. 989-1001, 2006.

[12] H. Barninghausen et al, "The crystal structure of A-Ce_2O_3," *Journal of the Less Common Metals,* vol. 110, no. 1-2, pp. 385-390, 1985.

[13] E. A. Kummerle et al, "The structure of C-Ce_2O_3-d, Ce_7O_{12} and $Ce_{11}O_{20}$," *Journal of Solid State Chemistry,* vol. 147, pp. 485-500, 1999.

[14] S. S. Kim, "Thermodynamic modeling of the CeO_2-CoO nano-phase diagram," *Journal of Alloys and Compounds,* vol. 588, pp. 697-704, 2014.

[15] P. J. Spencer, "Computational thermochemistry: from its early Calphad days to a cost-effective role in materials development and processing," *Calphad,* vol. 25, no. 2, pp. 163-174, 2001.

[16] M. Bekheet et al, "On the structure stability of crystalline ceria phases in undoped and acceptor-doped ceria materials under in situ reduction conditions," *CrystEngComm,* vol. 21, no. 1, pp. 145-154, 2019.

[17] G. B. Della Mea et al, "Tuning the oxygen vacancy population of cerium oxide (CeO_{2-x}, $0 < x < 0.5$) nanoparticles," *Applied Surface Science,* vol. 422, pp. 1102 - 1112, 2017.

[18] M. Avrami, "Kinetics of phase change. I General theory," *The Journal of Chemical Physics,* vol. 7, no. 12, pp. 1102-1112, 1939.

[19] M. Avrami, "Kinectics of phase change. II transformation-time relations for random distribution of nuclei," *The Journal of Chemical Physics,* vol. 8, no. 2, pp. 212-224, 1940.

[20] M. Avrami, "Granulation, phase change, and microstrucuture kinetics of phase change. III," *The Journal of Chemical Physics ,* vol. 9, no. 2, pp. 177-184, 1941.

[21] R. Kaischew et al, "Zur kinetischen Ableitung der Keimbildugsgeschwindingkeit," *Zeitschrifft fur Physikailische Chemie,* vol. 26, no. 1, pp. 317-326, 1934.

[22] Z. J. Yan et al, "On the cyrstallization kinetics of $Zr_{60}Al_{15}Ni_{25}$ amorphous alloy," *Journal of Alloys and Compounds,* vol. 368, pp. 175-179, 2004.

[23] . A. Jeziorny, "Parameters characterizing the kinetics of the non-isothermal crystallizattion of poly (ethylene terephthlate) determined by DSC.," *Polymer,* vol. 19, no. 10, pp. 1142-1144, 1978.

[24] L. Mandlekern, Crystallization of Polymer, New York: McGraw-Hill, 1964.

[25] A. Khawam, "Solid-State kinetic models: basics and mathematical fundamental.," *Journal of Physical Chemistry B,* vol. 110, no. 35, pp. 17315-17328, 2006.

[26] J. D. Hancock et al, "Method of comparing solid-state kinetic data and its application to the decomposition of kaolinite, brucite, and $BaCO_3$," *Journal of the American Ceramic Society,* vol. 55, no. 2, pp. 74-77, 1972.

[27] S. Hulbert, "Models foe solid state reactions," *Journal Brittish Ceramic Society,* vol. 6, pp. 11-20, 1969.

[28] K. S. Go et al, "Reaction kinetics of reduction and oxidation of metal oxides for hydrogen production," *International journal of hydrogen energy,* vol. 33, pp. 5986-5995, 2008.

[29] B. Bulfin et al, "Analytical model of CeO_2 oxidation and reduction," *The Journal fo Physical Chemistry C,* vol. 117, pp. 24129-24137, 117.

[30] Z. Zhinquan et al, "Kinetics of NiO reduction by H_2 and Ni oxidation att conditions relevant to chemical-looping combusting and reforming," *International Journal of Hydrogen Energy ,* vol. 39, pp. 8535-8556, 2014.

[31] H. Winick et al, Synchrotron radiation research, Springer Science & Business Media, 2012.

[32] B. D. Cullity et al, Elements of X-Ray Diffraction, Person Education, 2014.

[33] Website: www.psi.ch/sites/default/files/import/sing/dmc/ManualsEN/fullprof.pdf. Acessed in 5/20/2020.

[34] P. T. Andrews, Unoccupied electronic states: fundamentals for XANES, EELS, IPS and Bis, Berlin: Springer, 1992.

[35] J. J. Rehr, "Progress in theory and interpretation of XANES," *Coordination Chemistry Review,* vol. 249, pp. 131-140, 2005.

[36] L. Galoisy, "High-resolution XANES spectra of iron in minerals and glasses structural information from the pre-edge region," *Chemical Geology,* vol. 174, pp. 307-319, 2000.

[37] A. S. Thill et al, "Key role played by metallic nanoparticles on the ceria reduction," *The Journal of Physical Chemistry C,* vol. 121, no. 45, pp. 2523 - 25332, 2017.

[38] T. A. Assefa, "Tracking Chemical Reaction with Ultra fast X-ray Spectroscopy Techniques," Dissertation Universty of Hamburg, Hamburg, 2016.

[39] M. R. Pinton, Síntese e caracterização do composto $SrTi_{1-x}Mn_xO3$ nanestruturados, São Paulo: Tese de doutorado, Universidade de São Paulo.

[40] Website: https://www.lnls.cnpem.br/facilities/dxas-en/. Accessed in 8/31/2020.

[41] J. C. Cezar et al, "Energy-dispersive X-ray absorption spectroscopy at LNLS: investigation on strongly correlated metal oxides," *Journal of Synchrotron Radiation*, vol. 17, no. 1, pp. 93-102, 2010.

[42] D. B. Williams and C. B. Carter, Transmission Electron Microscopy: a textbook for materials science, Springer Science + Business Media, LLC, 1996.